Microfluid Nanofluid (2016) 20:36
DOI 10.1007/s10404-016-1704-7

RESEARCH PAPER

Combining molecular dynamics and lattice Boltzmann simulations: a hierarchical computational protocol for microfluidics

Aline O. Pereira[1] · **Lucas S. Lara**[1,3] · **Caetano R. Miranda**[1,2]

Received: 6 June 2015 / Accepted: 6 January 2016 / Published online: 23 January 2016

Abstract A hierarchical computational protocol is introduced to investigate the role of interfacial and wetting properties to the fluid displacement in hydrophilic pore network models (PNMs). Based on the combination of molecular dynamics (MD) and lattice Boltzmann method (LBM) simulations at both nano- and microscales, we study the role of dispersed functionalized SiO_2 nanoparticles (NP) in brine to the oil displacement process in a clay (montmorillonite—MMT) pore structure. Our MD calculations indicate that dispersion of NP, with different hydrophilic properties, in brine solution reduces the interfacial tension between oil and brine, followed by an increase in the contact angle. The lowest interfacial tension and highest contact angle are for the hydrophilic NP functionalized with polyethylene glycol groups. By mapping the properties obtained from MD into LBM simulation parameters, we explore the oil displacement process in hydrophilic PNMs at the microscale. For all systems, the Young–Laplace filling rules are obeyed and, due to the finger formation, the displacement efficiency decreases as the capillary number increases. It was observed that, with the inclusion of NP, a reduction in interfacial tension associated with an increase in the contact angle may enhance the oil displacement process in hydrophilic pore systems at the microscale. The proposed computational protocol can be a versatile tool to explore the potentialities of chemical additives, such as NP, for the oil recovery process and investigate the effects of interfacial tension and wetting properties on the fluid behavior at both nano- and microscales.

Keywords Hierarchical computational protocol · Lattice Boltzmann method · Molecular dynamics · Interfacial tension · Wettability · Fluid displacement

1 Introduction

The fluid–fluid interfacial and wetting properties play a crucial role in several physical processes and are of great importance for a broad range of technological applications such as enhanced oil recovery process, drug delivery, fuel cells, and environmental, pharmaceutical, biological and cosmetics technologies, among others (Bonn et al. 2009; Hore et al. 2008; Chandler 2007; Jungwirth et al. 2006; Benjamin 1997; Amott 1956). Therefore, the understanding and control of the physical and chemical processes underlying fluid–fluid interfaces are essential to the development and improvement of such technologies.

Despite the recent advances in experimental techniques, the determination of the interfacial tension and wetting properties at nanoscale continues to be a challenge (Lambert 2009; Nomoto and Onishi 2007; de Serio et al. 2006; Scatena et al. 2001; Mitrinovic et al. 2000; Du et al. 1994). For instance, most of the studies involving the free energy

---

Electronic supplementary material The online version of this article (doi:10.1007/s10404-016-1704-7) contains supplementary material, which is available to authorized users.

✉ Caetano R. Miranda
cmiranda@if.usp.br

[1] Nanopetro, Centro de Ciências Naturais e Humanas (CCNH), Universidade Federal do ABC, Av. dos Estados 5001, Santo André 09210-580, Brazil

[2] Present Address: Department of Mechanics and Materials Physics, Institute of Physics, University of São Paulo (USP), Rua do Matão, Travessa R, Nr 187, Cidade Universitária, São Paulo 05508-090, Brazil

[3] Present Address: Departamento de Física, Universidade Estadual de Ponta Grossa (UEPG), Av. Carlos Cavalcanti 4748, Ponta Grossa 84030-900, Brazil

of the interfaces do not include the size effects and surface morphology (Zhang et al. 1995; Michael and Benjamin 1995). In this case, molecular dynamics simulations (MDs) are a robust alternative to determine interfacial properties (de Lara et al. 2012a; Biben and Joly 2008; Buckley 2007; Navrotsky 2003). Moreover, MD can provide useful information about the underlying molecular mechanisms behind the wetting process and other physical properties of fluids such as structural and transport.

A review by Li et al. (2010) demonstrates the ability of MD to simulate liquid flow at the nanoscale. In MD simulations, the fluid behavior is described by the motion of the individual particles interacting with each other via intermolecular potentials (Koplik and Banavar 1995). As a consequence, a considerable computational cost limits its application to the nanoscale (*ns* and *nm*), and it is not possible to determine the fluid behavior at larger scales. To address this issue, one may resort to macroscopic methods like the lattice Boltzmann method (LBM), which is a kinetic theory model that intrinsically incorporates macroscopic and microscopic physical mechanisms (Sukop and Throne 2006; Succi 2001; Chen and Doolen 1995).

LBM simulations present several advantages for computational microfluidics, since they allow the simulation of complex fluid systems (Zhang 2011). These simulations have a solid theoretical foundation, and the algorithm is practical and suitable for flow simulations within high complex solid geometries. Additionally, phenomena like phase separation, interface instability, bubble/droplet dynamics and wetting effects can be successfully described (Wörner 2012).

In order to go beyond the nanoscale, we propose a hierarchical computational protocol that maps the fluid information obtained with MD into LBM flow simulations. As an example, we investigate the role of dispersed functionalized SiO_2 nanoparticles in brine to the oil displacement process in hydrophilic pore network models. The use of disperse solutions of nanoparticles has shown the ability to modify the interfacial properties of liquid–liquid systems and consequently the wettability when in contact with a solid surface. In fact, experimental results have shown that functionalized SiO_2 nanoparticles dispersed in brine solution can modify the brine/oil/rock properties (de Lara et al. 2012b; McElfresh et al. 2012; Zhang et al. 2010; Sondjaja et al. 2008; Wasan and Nikolov 2003).

SiO_2 nanoparticles (hydroxylated nanoparticles) are designed to be hydrophilic; however, their hydrophilic properties can be tuned by the graft of functionals to its surface (Rigo et al. 2014; Zhang et al. 2012). The resulting interfacial and wetting properties depend on the hydrophilicity of the functional used. In the present work, we consider functionalized nanoparticles with sulfonic acid (SA) and polyethylene glycol (PEG2), which lead to hydrophobic and hydrophilic characters, respectively (Rigo et al. 2014; Miranda et al. 2012).

Based on this, we use MD simulations to explore how the interfacial tension and wetting properties of the brine/oil/montmorillonite system changes with the use of hydroxylated and functionalized SiO_2 nanoparticles dispersed in brine (brine+NP) solution. After that, a mapping of the MD information into LBM parameters is performed, and we investigate how the oil displacement process is modified by the induced changes in the interfacial tension and wettability due to the inclusion of hydrophilic and hydrophobic nanoparticles.

2 Molecular dynamics simulations

Molecular dynamics simulations were carried out in the Large Atomic/Molecular Massively Parallel Simulator (LAMMPS) package (Plimpton 1995). The size of the initial simulation box is $12.3 \times 12.8 \times 8\ \text{nm}^3$, which is composed of two parallel montmorillonite (MMT) surfaces separated by an empty space of 8 *nm*. In order to create a brine–oil interface, the left side of the box is filled with an API brine solution (8 % NaCl and 2 % $CaCl_2$), while the right side contains the crude oil model (Miranda et al. 2012; de Lara et al. 2012a). For the brine+NP/oil/MMT systems, a spherical void is created at the central part of the brine–oil interface where a nanoparticle is added. A schematic representation of the computational boxes for such systems is presented in Fig. 1a, c).

Details about the potentials and structures considered in our simulations are presented in the following:

Montmorillonite (MMT) is a hydrophilic dioctahedral smectite clay with a monoclinic symmetry. It is characterized by the substitution of a Mg atom on the octahedral sheet by an Al atom, and by the substitution of an Al atom in the tetrahedral sheet by an Si atom. The most favorable sites for Mg and Al substitutions were identified using static energy minimization calculations. Each MMT surface was modeled as proposed by Cygan et al. (2012) and has the (1 0 0) crystallographic orientation. A supercell with a composition of $Na_3(Si_{31}Al)(Al_{14}Mg_2)O_{80}(OH)_{16}$ was used, which reproduces the typical composition for the Na smectite clay (Brindley and Brown 1980). Atomistic interactions were described within the CLAYFF potential (Cygan et al. 2012).

SiO_2 *nanoparticles* were generated using the Monte Carlo scheme proposed by Makimura et al. (2010). Based on amorphous SiO_2 atomistic sample, nearly spherical hydroxylated nanoparticles (NP–H) are obtained with a diameter of approximately 3 *nm*, in agreement with exper-

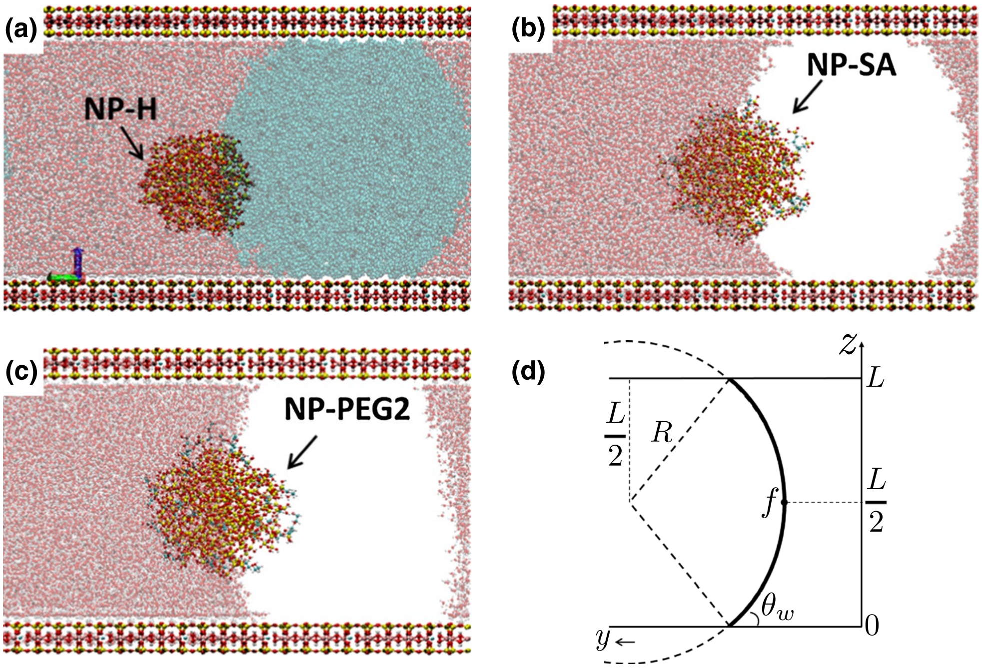

Fig. 1 Schematic representations at the *yz*-plane of the computational boxes for the brine+NP/oil/MMT systems containing: **a** hydroxylated nanoparticle (NP–H), **b** sulfonic acid functionalized nanoparticle (NP-SA) and **c** polyethylene glycol functionalized nanoparticle (NP-PEG2). In figures (**b**) and (**c**), the oil molecules (*green color*) are omitted in order to obtain a better view of the functional groups at the nanoparticle's surface. **d** Diagram for the meniscus formed by a liquid–liquid interface confined between two surfaces located at $z = 0$ and $z = L$. The meniscus is denoted by the function *f*. *R* is the meniscus' curvature radius, while θ_w is the contact angle (color figure online)

imental and theoretical studies (Metin et al. 2014; Song and Choi 2002). In order to reproduce the experimental observations of Murray (2010), the surface of NP–H is composed by 83 % of Si(OH) and 17 % of $Si(OH)_2$ terminations. Such surface configuration ensures a hydrophilic character to NP–H. In the case of functionalized nanoparticles, part of these silanol groups at the surface is replaced by a new functional group: (i) hydrophobic sulfonic acid $(Si(OH)_3 - (CH_2)_3 - SO_3H)$ or (ii) hydrophilic polyethylene glycol $(Si(OH)_3 - (O - CH_2 - CH_2 - O)2 - H)$. The number of functional groups in the nanoparticle surface was previously determined by means of first principles calculations (Rigo et al. 2014). A CHARMM-based interatomic potential proposed by Cruz-Chu et al. (2006) and a non-rigid bulk modification (Rigo et al. 2014) were used to describe the SiO_2 nanoparticles.

Brine solution is composed of 16000 water molecules and the appropriated number of ions to obtain an API solution (8 % of NaCl and 2 % $CaCl_2$). The water molecules were described by the SPCE/FH potential (Alejandre et al. 2009). This is a three-point charge model with van der Waals and Coulomb interaction terms. Flexible internal degrees of freedom are also considered, i.e., $O - H$ harmonic bond stretching and $H - O - H$ harmonic angle bending terms. Na, Ca and Cl interact only via van der Waals and Coulomb interactions. The Coulomb and long-range parameters were the same used by Gavryushov (2007).

Oil is described by the light crude oil model, where alkanes and aromatics hydrocarbons are considered. The number of alkanes molecules in our computational box is: 144 hexane, 132 heptane, 156 octane, 180 nonane, 96 cyclohexane and 156 cycloheptane. In the case of aromatic hydrocarbons, 156 toluene and 60 benzene molecules are considered. All hydrocarbons were described by the CHARMM-based force fields (Brooks et al. 2009). This crude oil model has been previously studied by Miranda et al. (2012); de Lara et al. (2012a) and Kunieda et al. (2010).

To equilibrate the systems, a sequence of NVE, NVT and NPT simulations at 300 *K* and 1 *atm* were carried out for 1 *ps*, 10 *ps* and 2 *ns*, respectively. Periodic boundary conditions have been applied. The long-range electrostatic interactions were treated using the Particle–Particle–Particle–Mesh (PPPM) method (Thompson et al. 2009; Jang et al. 2004; Hockney 1989), and the Lorentz–Berthelot mixing rules were employed (Berthelot 1898; Lorentz 1881). A time step of 0.5 *fs* and a cutoff radius of 10 Å for van der Waals and Coulomb interactions were considered. The control of temperature was performed using the Nosé–Hoover thermostat (Hoover 1985; Nosé 1984), while the pressure was controlled by the Andersen barostat (Andersen 1980). During the calculation, the structure of the MMT surface is preserved by fixing the x- and y-directions of the computational box $(12.3 \times 12.8)\,\mathrm{nm}^2$. On the other hand, the z-direction (perpendicular to the MMT (1 0 0) surface) was allowed to relax in order to accommodate the different nanoparticles. The equilibrium size in the z-direction for the brine/oil/MMT system is 7.7 *nm*. For systems containing nanoparticles, the equilibrium sizes are 7.5, 7.2 and 7.2 *nm* for NP-H, NP-SA, and NP-PEG2, respectively. After equilibration, the averaged density, viscosity, interfacial tension, and the contact angle were measured over a 4-ns simulation within the NVT ensemble.

The dynamic viscosity μ of each fluid was measured based on the Green–Kubo (Kubo 1957; Green 1954) formalism, which relates the fluid viscosity to the ensemble average of the pressure tensor auto-correlation function. Therefore,

$$\mu = \frac{V}{k_\mathrm{B} T} \int_0^\infty \mathrm{d}t \left\langle P_{ij}(0) P_{ij}(t) \right\rangle. \tag{1}$$

In this equation, P_{ij} are the non-diagonal terms of the pressure tensor that can be along the xy-, yz- or xz-directions, V is the fluid's volume and T is the temperature of the system. In addition, the kinematic viscosity of the fluid is defined as $\nu = \mu/\rho$.

The interfacial tension was calculated within the Gibbs formulation in terms of the pressure tensor (Ghoufi et al. 2008; Jang et al. 2004; Varnik et al. 2000; Evans and Morriss 1990)

$$\gamma = \frac{1}{2} \int_{-L_b}^{L_a} \mathrm{d}y \left[p_{ab}(y) - p_T(y) \right]. \tag{2}$$

The parameters L_a and $-L_b$ determine the distance limits of the interfacial area, and p_{ab} and p_T are the normal and tangential components of the pressure tensor, respectively. The y-direction is normal to the interface and parallel to the MMT (1 0 0) surface, as shown in Fig. 1d. The calculation of the per-atom virial (pressure tensor) was done by following the implementation within the Lammps code (Thompson et al. 2009; Plimpton 1995).

The contact angle θ_w was determined by using the geometric method (Boukellal et al. 2009). When there is a formation of a meniscus at the liquid–liquid interface, as shown in Fig. 1d, the contact angle can be defined as follows

$$\theta_w = \arcsin \left[\frac{L}{2R} \right], \tag{3}$$

where R is the curvature radius of the meniscus and L is the distance between the two surfaces located at $z = 0$ and $z = L$.

3 Lattice Boltzmann simulations

The fluid flow is modeled within the explicit forcing lattice Boltzmann model (EF-LBM) proposed by Porter et al. (2012). This is a multicomponent interparticle-potential LBM for immiscible fluids with large viscosity ratios, where the external forces are directly incorporated into the discrete Boltzmann equation.

The dynamics of a fluid mixture containing k fluid components is described by a set of particle distribution functions $f_i^k(\mathbf{x}, t)$ on a discrete two-dimensional lattice connected by nine velocity vectors $\mathbf{e}_i$ (D2Q9 lattice; Wolf-Gladrow 2000). Each distribution function satisfies the discrete Boltzmann equation

$$\begin{aligned} & f_i^k(\mathbf{x} + \mathbf{e}_i \Delta t, t + \Delta t) - f_i^k(\mathbf{x}, t) \\ & \quad = \frac{1}{\tau_k} \left[f_i^{eq,k}(\mathbf{x}, t) - f_i^k(\mathbf{x}, t) - \frac{\Delta t}{2} f_i^{F,k} \right] + \Delta t f_i^{F,k}. \end{aligned} \tag{4}$$

where τ_k is the dimensionless relaxation time for each fluid component, which is related to the kinematic viscosity by $\nu_k = (\tau_k - 0.5)/3$. The equilibrium particle distribution function $f_i^{eq,k}$ and the forcing terms $f_i^{F,k}$ have the same form as implemented by Porter et al. (2012).

The forcing terms are responsible to introduce changes due to the total force acting on each fluid component. They are able to capture distinct physical effects, including external body forces such as gravity, internal forces such as inter-particle potentials (surface tension), and cohesive forces to solid surface (fluid wettability).

The inter-particle potentials are introduced via fluid–fluid forces:

$$\mathbf{F}_{ff}^k = -\rho_k(\mathbf{x}) \sum_{k'=1}^{n_k} \sum_{x' \in \mathcal{N}_x} \mathcal{G}_{k,k'}\left(|\mathbf{x}' - \mathbf{x}| \right) \frac{\rho_k(\mathbf{x}') - \rho_k(\mathbf{x})}{|\mathbf{x}' - \mathbf{x}|} \left(\mathbf{x}' - \mathbf{x} \right). \tag{5}$$

The second summation is taken over a set of lattice sites $\mathcal{N}_x$ which do not include wall sites and whose direct path from $\mathbf{x}$ to $\mathbf{x}'$ is not blocked by wall sites. $\mathcal{G}_{k,k'} = g_{kk'} \hat{\mathcal{G}}$, where $g_{kk'}$ specifies the strength of forces and equivalently the surface tension, while $\hat{\mathcal{G}}$ enforces isotropy and spatial extent that increases the numerical stability and allows the simulation of fluid mixtures with high viscosity ratios. Such fluid–fluid forces enable phase separation and surface tension to be easily included in LBM.

As presented by Porter et al. (2012), there is a unique relationship between the surface tension and the interaction strength g_{12} of a binary mixture, which is independent of the chosen viscosity and viscosity ratio. Therefore, a simple quadratic fit $(\gamma_{12} = -1.361 g_{12}^2 + 1.721 g_{12} - 0.178)$ can be used as a tool to estimate the surface tension γ_{12} of a given binary mixture of any viscosity and viscosity ratio.

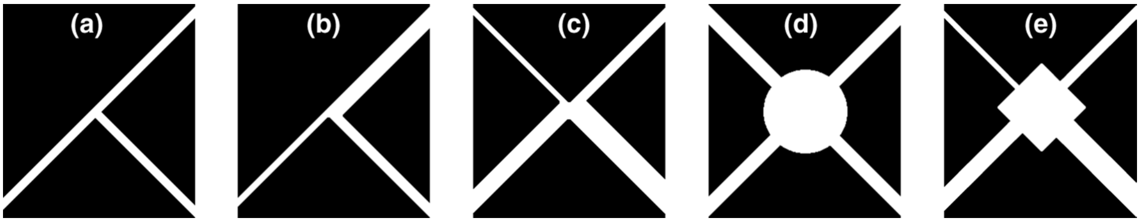

Fig. 2 Pore network models: **a** T-junction with equal channel widths; **b** T-junction with unequal channel widths; **c** X-junction with unequal channel widths; **d** X-junction with equal channel widths and circular pore body; **e** X-junction with unequal channel widths and square pore body. *Black regions* represent solid area, while the *white color* stands for pore space. The size of each pore network model is $5.68 \times 6.39\,\mu\text{m}^2$

Cohesive forces to solid surface are included through the fluid–solid forces:

$$\mathbf{F}_{fs}^{k} = -\rho_k(\mathbf{x}) \sum_{m=1}^{n_s} g_k^s \sum_{x' \in \mathcal{W}_s} (\mathbf{x}' - \mathbf{x}), \tag{6}$$

where g_k^s is the fluid component k's affinity for the solid and the summation is taken over a set of neighboring sites $\mathbf{x} + \mathbf{e}_i$ that represents a solid site.

The density of each fluid component and the fluid pressure are defined as follows

$$\rho_k = \sum_i f_i^k \tag{7}$$

and

$$p = \frac{1}{3} \sum_k \rho_k + 3 \sum_{kk'} g_{k,k'} \rho_k \rho_{k'}. \tag{8}$$

Our EF-LBM simulations were carried out in the open source software TAXILA LBM (Coon et al. 2014). For the solid structures, we consider a set of hydrophilic pore network models (PNM) as proposed by Chapmana et al. (2013). These models were chosen to understand the role of pore shape and throat width on fluid displacement (Ushikubo et al. 2014; Chapmana et al. 2013; Buckley 1991), as the interfacial and wetting properties are changed by the different displacing fluids. As can be seen in Fig. 2, they are composed of channel junctions with both equal and unequal widths, where a central pore body can be included or not.

It is expected that the fluid displacement sequence in PNM follows the Young–Laplace filling rules, i.e., channels with the lowest entry pressure are filled first by the displacing fluid (Chapmana et al. 2013). The entry pressure P_e determines the lowest pressure value that the fluid front of the injection fluid must have in order to enter the pore channel structure. It can be defined in terms of the Young–Laplace law (Buckley 1991; Lenormand et al. 1983)

$$P_e = 2\gamma \cos\theta_w \left(\frac{1}{h} + \frac{1}{w} \right), \tag{9}$$

where h and w are the height and width of the PNM channel, respectively. Therefore, the injection of a wetting fluid ($\theta_w < 90°$) leads to a positive entry pressure. By assuming that all channels have the same height, the lowest entry pressure is for the widest channel, which should be filled first.

The size of each PNM is $5.68 \times 6.39\,\mu\text{m}^2$ ($L_x \times L_y$), and is represented by a computational domain composed of 256×258 ($\tilde{L}_x \times \tilde{L}_y$) lattice units. A flux boundary condition (Coon et al. 2014) was imposed at the inlet (left side), where different values for the injection rate (u_0) are considered in order to obtain different capillary numbers ($Ca = \nu\rho u_0/\gamma$). Regarding the outlet (right side), a density boundary condition (Coon et al. 2014) was adopted. Periodic boundary conditions are employed at the top and bottom sides of the domain. At the lattice sites where the fluid meets a wall, a bounce-back boundary scheme (He et al. 1997) is used to achieve the nonslip velocity condition at the solid surface.

In order to illustrate the fluid displacement efficiency, the areal sweep efficiency number is calculated at the breakthrough time. The areal sweep number is the ratio of the displaced fluid (oil) volume being swept by the displacing fluid (brine or brine+NP) to the total pore volume. The breakthrough time is defined as the time when the displacing fluid front reaches the outlet area. In the numerical analysis, it is assumed that the fluid front has arrived the outlet when the maximum mass fraction of the displacing fluid at the outlet is larger than 0.5. A discussion about the error bars in the areal sweep number, due to MD simulation error bars, is presented in the supplementary material. It was found an error of ±0.003 in the areal sweep number.

4 Mapping from MD to LBM

By performing MD calculations, the physical properties of the brine/oil/MMT and brine+NP/oil/MMT system were

Table 1 Summary of the molecular dynamics results for density (ρ), kinematic viscosity (ν), interfacial tension (γ_{bo}) and contact angle (θ_w) at 1 atm and 300 K

System	Brine		Oil		Brine–oil	
	ρ_b (kg/m^3)	ν_b (10^{-6}m^2/s)	ρ_o (kg/m^3)	ν_o (10^{-6}m^2/s)	γ_{bo} (kg/s^2)	θ_w (°)
No NP	997	0.791	810	4.473	0.043	21
NP-H	1026	0.867	810	4.348	0.038	26
NP-SA	1037	0.867	810	4.395	0.033	33
NP-PEG2	1034	0.854	810	4.384	0.029	40

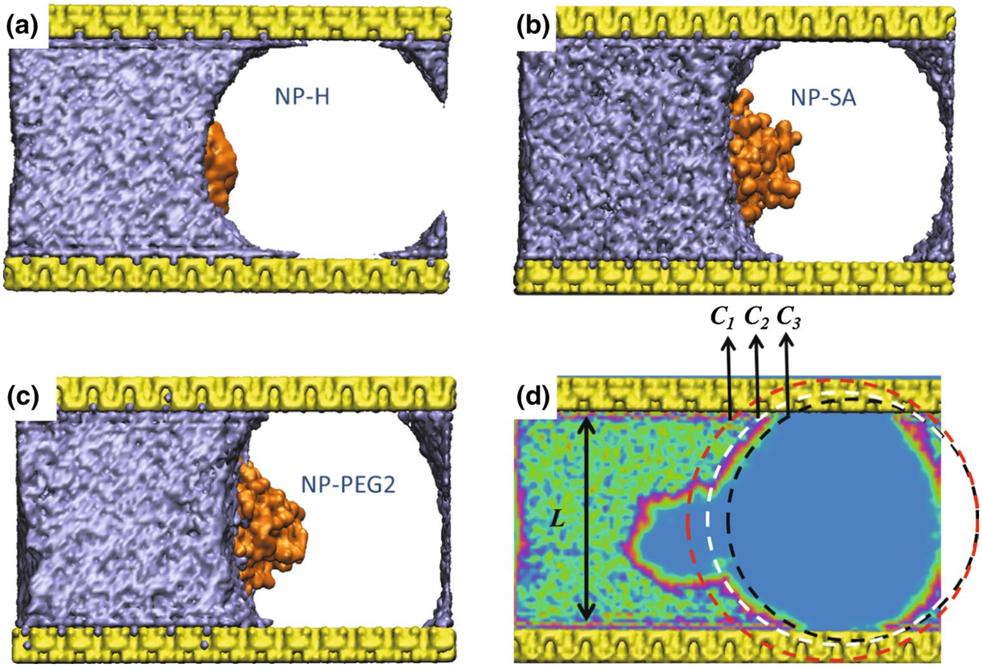

Fig. 3 2D projection of the volumetric density profiles for: **a** brine+NP-H/oil/MMT, **b** brine+NP-SA/oil/MMT and **c** brine+NP-PEG2/oil/MMT systems. Oil density was omitted in order to obtain a better view of the nanoparticles at the interface. **d** Representation of the proposed Gibbs dividing surfaces. C_1, C_2 and C_3 are circular sections in the *yz*-plane of the cylindrical Gibbs dividing surfaces. The circular section C_2 defines the meniscus at the brine–oil interface. L is the spacing between the two MMT surfaces

determined. The injection fluids are brine and brine+NP solution, where the NP-H, NP-SA and NP-PEG2 were considered. The determined densities and viscosities are shown in Table 1. Viscosities were calculated following the Green–Kubo formalism as defined in Eq. (1).

Figure 3a, c shows the 2D projection of the volumetric densities for the brine+NP/oil/MMT systems, in which the oil density was omitted for a better visualization of the nanoparticles at the interface. These results show that the shape of the meniscus formed by the brine–oil interface has a strong dependence on the type of nanoparticle added to the brine solution, which is associated with variations on the interfacial tension (γ_{bo}) and the contact angle (θ_w). Therefore, the influence of the addition of nanoparticles to the brine solution can be quantified by the determination of γ_{bo} and θ_w. To do so, the exact location of the interfacial meniscus is obtained by using the Gibbs dividing surface method (GDS) (Talu and Myers 2001; Chattoraj and Birdi 1984).

The GDS is defined as the spacial region where the excess of the brine constituents (H_2O, Na^+, Ca^{2+} and Cl^-) in the oil phase is approximately equal to the excess of oil molecules in the brine phase. Initially, we propose three different positions for the GDS, as shown in Fig. 3d. Due to the symmetry, proposed cylindrical GDS is represented by three circular sections (C_1, C_2 and C_3) at the *yz*-plane. By computing the surface excess in each phase, we conclude that the interface is well represented by the meniscus C_2. Now that the brine–oil interface is established, and the interfacial tension and the contact angle can be computed as defined in Eqs. (2) and (3). These results are also shown in Table 1 and indicate that the addition of nanoparticles to the brine solution reduces the interfacial tension between oil and brine, followed by an increase in the contact angle. Such properties may lead to a enhancement of the oil displacement process in hydrophilic pore structures.

As previously mentioned, the MD simulations are limited to the nanoscale (*nm* and *ns*) and the use of LBM simulations is required in order to extend how these changes in interfacial and wetting properties will affect the fluid behavior at the microscale. In our simulations, the solid nanoparticles are not explicitly included; thereby, the brine+NP solutions are treated as mean-field fluids with the same physical properties as the fully atomistic brine+NP solution (MD systems). Also, in order to do

Table 2 Dimensionless LBM parameters derived from the MD results shown in Table 1

System	τ_b	τ_o	$\tilde{\gamma}_{bo}$	g_{bo}	g_b^{MMT}
No NP	1.230	4.628	0.100	0.190	−0.045
NP-H	1.299	4.513	0.089	0.181	−0.056
NP-SA	1.300	4.556	0.077	0.171	−0.058
NP-PEG2	1.288	4.546	0.068	0.164	−0.057

The characteristic scale is: $l_0 = 2.22 \times 10^{-8}$ m, $t_0 = 1.52 \times 10^{-10}$ s and $m_0 = 9.91 \times 10^{-21}$ kg

avoid the effect of NP agglomeration and to keep the MD distribution of NP at the brine/oil interface, brine solutions with a low concentration of NPs are considered. Based on these assumptions, the following procedure was employed to map the computed MD physical properties of each system into LBM simulation parameters.

In LBM simulations, all variables are in lattice units, which can be related to physical units by a dimensionless conversion using the characteristic scale of the system (l_0, t_0, m_0). The characteristic scale of a system can be easily determined by defining three computational LBM parameters for one of the fluid components. In our case, we define the lattice size ($\tilde{L}_x = 256$), the oil density ($\tilde{\rho}_o = 1$) and the interfacial tension between oil and brine ($\tilde{\gamma}_{bo} = 0.1$). By performing a dimensional analysis, the characteristic scale can be determined as follows:

Characteristic length (l_0) is defined in terms of the sizes of the real system L_x and the computational domain $\tilde{L}_x$:

$$L_x = l_0 \times \tilde{L}_x \longrightarrow l_0 = L_x/\tilde{L}_x. \tag{10}$$

Characteristic mass (m_0) can be calculated through the real density ρ_o, dimensionless density $\tilde{\rho}_o$ and the characteristic length l_0:

$$\rho_o = \frac{m_0}{l_0^3}\tilde{\rho}_o \longrightarrow m_0 = \frac{\rho_o}{\tilde{\rho}_o} \times l_0^3. \tag{11}$$

Characteristic time (t_0) is determined by the real γ_{bo} and dimensionless $\tilde{\gamma}_{bo}$ interfacial tension and the characteristic mass m_0:

$$\gamma_{bo} = \frac{m_0}{t_0^2}\tilde{\gamma}_{bo} \longrightarrow t_0 = \left(\frac{\tilde{\gamma}_{bo}}{\gamma_{bo}} \times m_0\right)^{\frac{1}{2}}. \tag{12}$$

For our systems, the characteristic scales are found to be $l_0 = 2.22 \times 10^{-8}$ m, $t_0 = 1.52 \times 10^{-10}$ s and $m_0 = 9.91 \times 10^{-21}$ kg. All the other computational parameters can be defined via a dimensionless conversion using the characteristic scale. Table 2 shows a summary of the LBM parameters derived from the MD results presented in Table 1.

The oil–brine interaction strengths g_{bo} were computed in terms of the interfacial tension $\tilde{\gamma}_{bo}$ and the simple relation $\tilde{\gamma}_{bo} = -1.361g_{bo}^2 + 1.721g_{bo} - 0.178$ (Porter et al. 2012). The determination of the wetting parameters $g_o^{MMT} = -g_b^{MMT}$ requires a set of calculations for the brine–oil and brine+NP-oil interfaces in a MMT channel. For each calculation, a different value of g_b^{MMT} was used and the contact angle was measured using the geometric method, defined in Eq. (3). This process is repeated until the measured contact angle fits the MD value.

A benchmark example of the proposed hierarchical computational protocol is presented in the supplementary material. We explore the brine flux inside a MMT channel and compare the velocity profiles for both MD and LBM simulations.

5 Fluid displacement in hydrophilic pore network models

In this section, we explore the oil displacement process in the hydrophilic MMT pore network models shown in Fig. 2. We investigate the oil displacement by brine and brine+NP solutions in PNMs structures with equal and unequal channel widths. The effects of the inclusion of central pore bodies were also analyzed. In addition, we also investigate the different fluid injection rates (0.003, 0.005, 0.007 and 0.009 l_0/t_0), which leads to similar injection profiles; for this reason, the results for 0.005, 0.007 and 0.009 l_0/t_0 were omitted.

5.1 T-Junction models

We begin our analysis by the oil displacement in the T-junction model with narrow equal channel widths (Fig. 2a). The injection profiles are quite similar for all considered injection fluids: (i) brine, (ii) brine+NP-H, (iii) brine+NP-SA and (iv) brine+NP-PEG2. Therefore, results only for the brine+NP-PEG2 injection are shown in Fig. 4a. Four different time snapshots of the fluid densities are shown, where the red, green and blue colors represent the brine+NPPEG2, oil and MMT, respectively. As a consequence of the symmetrical characteristic of the pore structure, a similar entry pressure is observed for both channels and the injected fluid enters both channels in a similar way. After 17.16 µs of injection, almost all of the oil content is displaced, leading to an areal sweep efficiency number of 0.980.

Although the injection profiles are similar for the different injection fluids and injection rates, this is not the case for the areal sweep efficiency. Figure 4b shows the areal sweep efficiency number as a function of the capillary number for the different injection fluids at the breakthrough

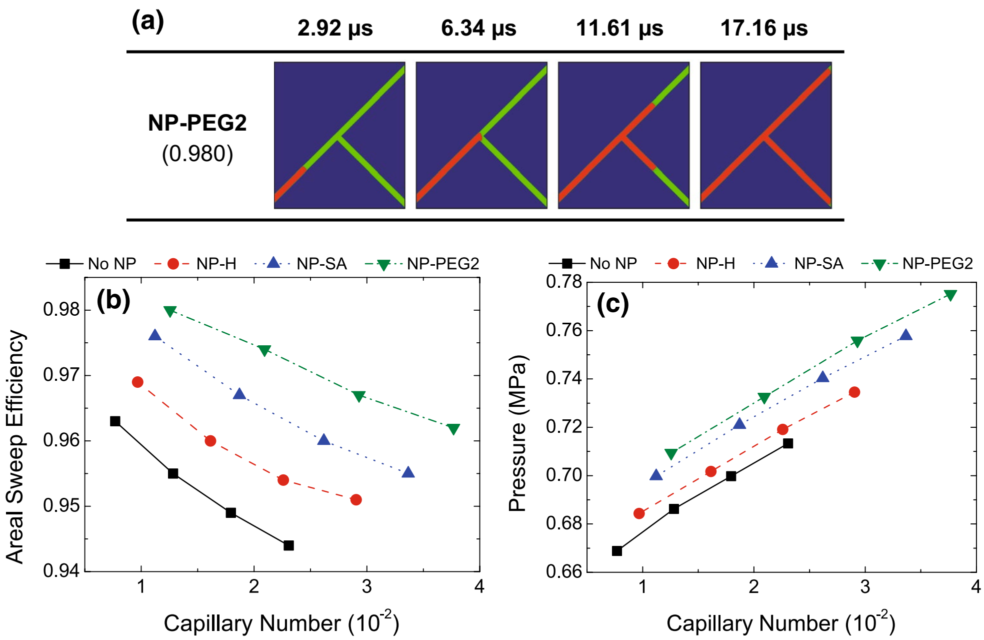

Fig. 4 T-junction pore network model with equal narrow channel widths. **a** Injection profile for a brine+NP-PEG2 (*red*) solution into a MMT (*blue*) pore network filled with oil (*green*). Injection rate is 0.003 l_0/t_0. For this system, an areal sweep efficiency of 0.980 is attained after 17.16 µs of injection. **b** Areal sweep efficiency as a function of the capillary number. **c** Pressure at the interface. The injection fluids are: (*square*) brine, (*circle*) brine+NP-H, (*up triangle*) brine+NP-SA and (*down triangle*) brine+NP-PEG2. These results are computed at the breakthrough time for brine+NP-PEG2 injection (color figure online)

time for brine+NP-PEG2 injection. These results indicate that, independently of the injection rate, the addition of nanoparticles within brine solution indeed improves the oil displacement process, i.e., increase the areal sweep efficiency number in relation to a pure brine injection (square data in Fig. 4b). The maximum improvement is obtained for a brine+NP-PEG2 solution, where the displacement efficiency is increased by approximately 2 %. Also, a decrease in the areal sweep efficiency is seen as the capillary number increases, which is probably related to differences in the shape of the displacing fluid front (brine or brine+NP). Even though the formation of fingers at the fluid front is expected for large injection rates, the finger formation is not observed. This is a consequence of the large entry pressure associated with the narrow channels that balances the injection force and does not allow the finger formation. Moreover, such effect may explain the observed similar injection profiles.

The pressure values at the interface were also analyzed. The interfacial pressure as a function of the capillary number for the different injection fluids at the breakthrough time for brine+NP-PEG2 injection is shown in Fig. 4c. Owing to the symmetry of the pore model, similar interfacial pressures are obtained for both channels. The use of a brine solution with dispersed SiO$_2$ nanoparticles, as well as the increase in capillary number, leads to an increase in the interfacial pressure.

In order to investigate the effects of different entry pressures, we study the oil displacement in a T-junction PNM with unequal channel widths. Similarly to what is found for the T-junction model with equal channel widths (Fig. 4a), the injection profiles are quite similar for all considered injection fluids. This way, Fig. 5a shows only the results for the brine+NP-PEG2 injection. Differently from what is seen for the system with equal channel widths, in this case the oil displacement is 4.89 µs slower. Also, the time snapshots suggest that the Young–Laplace filling rules are satisfied, i.e., as a consequence of a lower entry pressure, the widest channel is filled first and faster than the narrow one. By the time that the brine solution reaches the outlet area of the widest channel, a considerable amount of oil is left at the narrow channel, which results in a lower areal sweep efficiency of 0.791 in comparison with the system with equal widths.

The areal sweep efficiency number as a function of the capillary number for the different injection fluids and rate is shown in Fig. 5b. These values are computed at the breakthrough time for brine+NP-PEG2 injection. Again, the addition of SiO$_2$ nanoparticles to the brine solution increases the areal sweep number in relation to the pure brine solution. The best displacement efficiency is seen for NP-PEG2 system, where an increase in approximately 2.5 % is obtained. In agreement to what is observed for the T-junction model with equal widths, the areal sweep

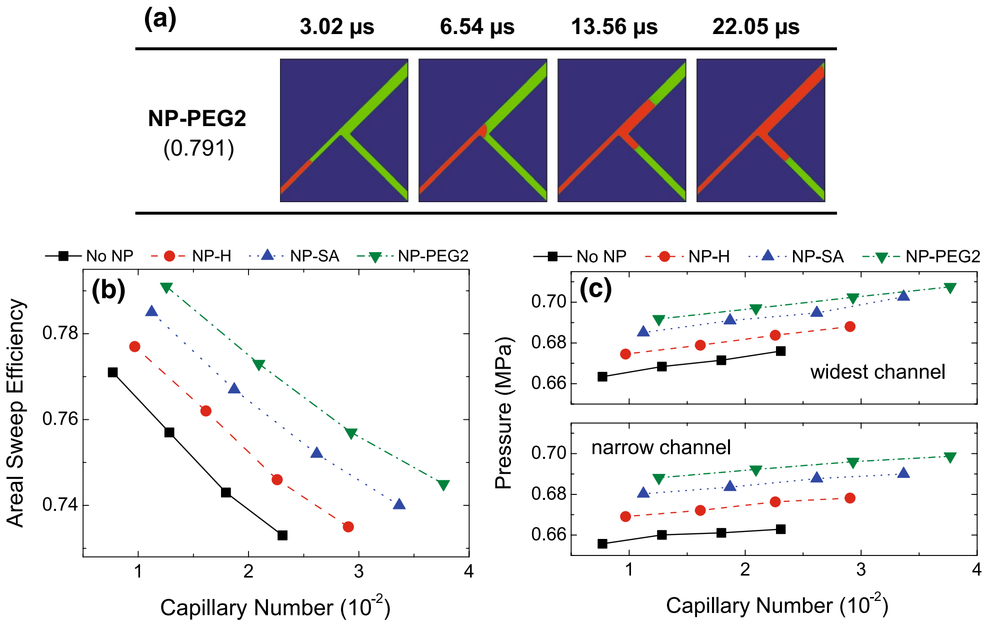

Fig. 5 T-junction pore network model with unequal channel widths. **a** Injection profile for a brine+NP-PEG2 (*red*) solution into a MMT (*blue*) pore network filled with oil (*green*). Injection rate is 0.003 l_0/t_0. For this system, an areal sweep efficiency of 0.791 is attained after 22.05 μs of injection. **b** Areal sweep efficiency as a function of the capillary number. **c** Pressure at the interface. The injection fluids are: (*square*) brine, (*circle*) brine+NP-H, (*up triangle*) brine+NP-SA and (*down triangle*) brine+NP-PEG2. These results are computed at the breakthrough time for brine+NP-PEG2 injection (color figure online)

number decreases with the capillary number as a result of different injection fluid fronts.

Figure 5c shows the interfacial pressure as a function of the capillary number for the different injection fluids at the breakthrough time for brine+NP-PEG2 injection. As a consequence of the different channel widths, the interfacial pressure is different at each one of the outlet channels. In agreement with the Young–Laplace's filling rule, the interfacial pressure is higher in the widest channel. In this case, at the widest channel, the entry pressure is lower, while the interfacial pressure is higher. Since the opposite is seen at the narrow channel, the widest channel is filled first. Similar to what is found for the T-junction model with equal widths, the addition of nanoparticles to the brine solution, as well as the increase in capillary number, leads to an increase in the interfacial pressure.

5.2 X-Junction models

The oil displacement process in the X-junction model with unequal channel widths allows us to also investigate the effects of two different injection sources. As can be seen in Fig. 2c, the inlet and outlet parts are composed of one narrow and one larger channel. The time snapshots for the brine and brine+NP injection process are shown in Fig. 6a. Differently from what is seen for the T-junction models (Figs. 4a, 5a), the injection density profiles considerably change from one injection fluid to another. After 2.24 μs of injection, it is possible to see that, at the inlet part, the fluid displacement is faster for the wider channel, in which the injection fluid front reaches the central part of the PNM first (5.66 μs). At this point, the injection follows the Young–Laplace filling rules and the widest channel located at the outlet part is filled first. The largest width of the outlet channel allows the formation of a finger front, as can be seen from the time snapshots at 8.10 and 10.54 μs. This happens because as the width of the channel increases, the entry pressure is reduced, and as a consequence, the injection force is predominant, which leads to the fingering formation.

By comparing the oil displacement process for the different brine solutions, one may conclude that the use of brine+NP-SA and brine+NP-PEG2 solutions leads to a faster displacement than that by the other injection fluids. For brine+NP-H and pure brine solutions, the breakthrough time is of about 11.71 μs, which is 1.17 μs slower. It is also a consequence of the predominance of the injection force over the entry pressure. Since the injection force is stronger, the differences in interfacial tension become more significative; systems with lower interfacial tension (brine+NP-SA and brine+NP-PEG2) will result in more pronounced finger formation and faster fluid displacement. This effect is also reflected in the areal sweep efficiency; after 10.54 μs of injection, the largest areal sweep numbers are for brine+NP-SA (0.771) and brine+NP-PEG2 (0.779).

Figure 6b shows the areal sweep efficiency number as a function of the capillary number for the different injection fluids and rates. These values are computed at the breakthrough time for brine+NP-PEG2 injection. In a similar way to the previous systems, an improvement in oil displacement is seen for injection fluids with nanoparticles. For a brine+NP-PEG2 solution, the fluid displacement efficiency increases more than 3 %. For all injection fluids,

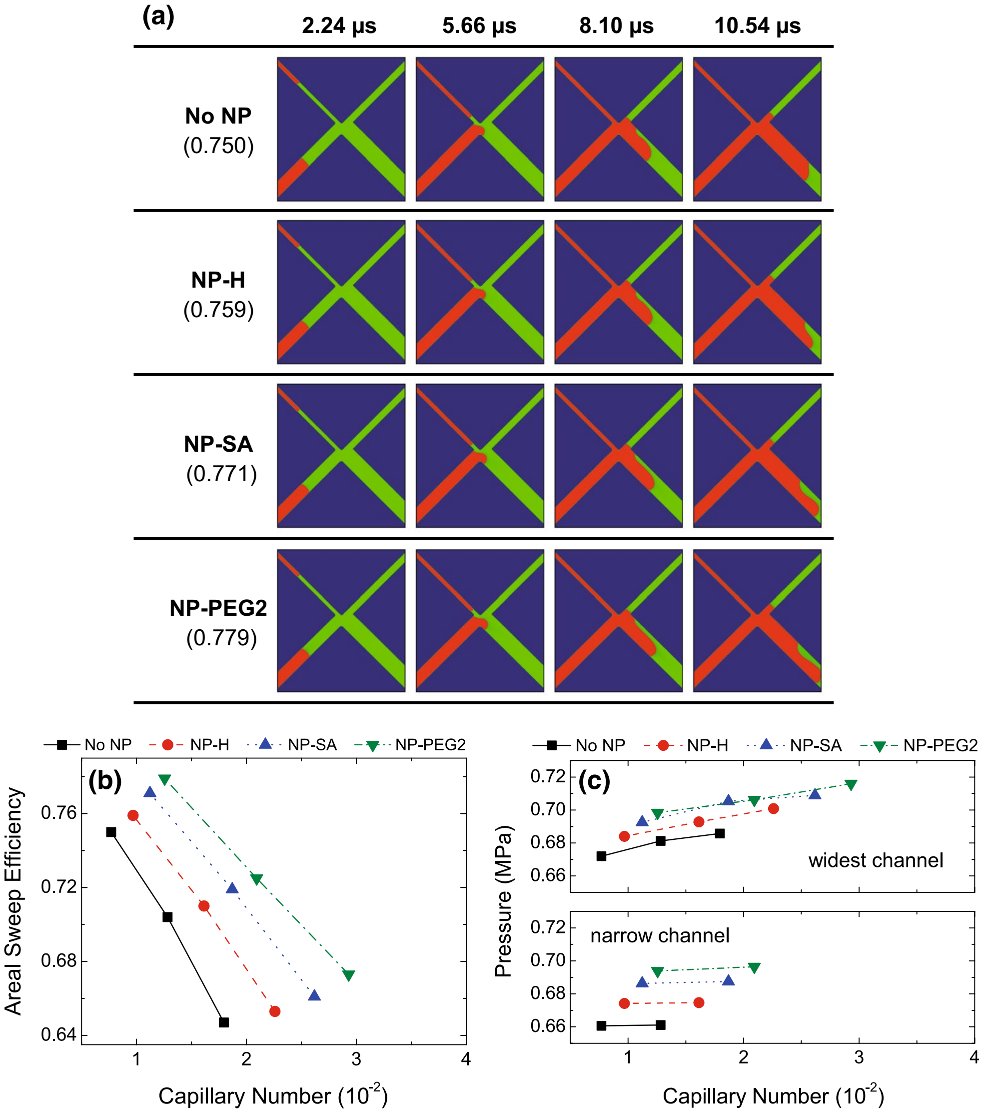

Fig. 6 X-junction pore network model with unequal channel widths. **a** Injection profiles for brine+NP (*red*) solutions into a MMT (*blue*) pore network filled with oil (*green*). Injection rate is 0.003 l_0/t_0, and the areal sweep efficiency attained after 10.54 μs of injection is shown in parenthesis. **b** Areal sweep efficiency as a function of the capillary number. **c** Pressure at the interface. The injection fluids are: (*square*) brine, (*circle*) brine+NP-H, (*up triangle*) brine+NP-SA and (*down triangle*) brine+NP-PEG2. These results are computed at the breakthrough time for brine+NP-PEG2 injection (color figure online)

as the capillary number increases, the areal sweep efficiency decreases. Simulations for a relatively large injection rate (0.009 l_0/t_0) lead to numerical instabilities and are not shown in this work. This instabilities arise due to the presence of spurious velocities near the interface in narrow channels and can be avoided in 3D simulations.

Results for the interfacial pressure are also presented, Fig. 6c. These values are computed for at the breakthrough time for brine+NP-PEG2 injection at the outlet channels. Information about the interfacial pressure at the narrow channel for an injection rate of 0.007 l_0/t_0 is not shown, since the fluid front does not attain the narrow channel area. In accordance with the previous results, the interfacial pressure increases with the addition of nanoparticles and the increase in the injection rate. Also, the largest observed interfacial pressure is for the widest channel, in agreement with the Young–Laplace's filling rule.

We proceed our analysis by investigating the effects of the inclusion of a central pore body to the PNM structure. Figure 7a shows the time snapshots for the oil displacement in the X-junction model with equal channel widths and a circular pore body. In agreement with what is found for the X-junction model with unequal channel widths (Fig. 6a), the oil displacement process by brine+NP-SA and brine+NP-PEG2 solutions is slightly faster than that by the other injection fluids. For brine+NP-H and pure brine solutions, the breakthrough time is of about 14.63 μs, which is 0.68 μs lower. Again, this is a consequence of the predominance of the injection force over the entry pressure, and systems with lower interfacial tension (brine+NP-SA and brine+NP-PEG2) will result in more pronounced finger formation and faster fluid displacement. After 13.95 μs of injection, the largest areal sweep numbers are for brine+NP-SA (0.857) and brine+NP-PEG2 (0.871).

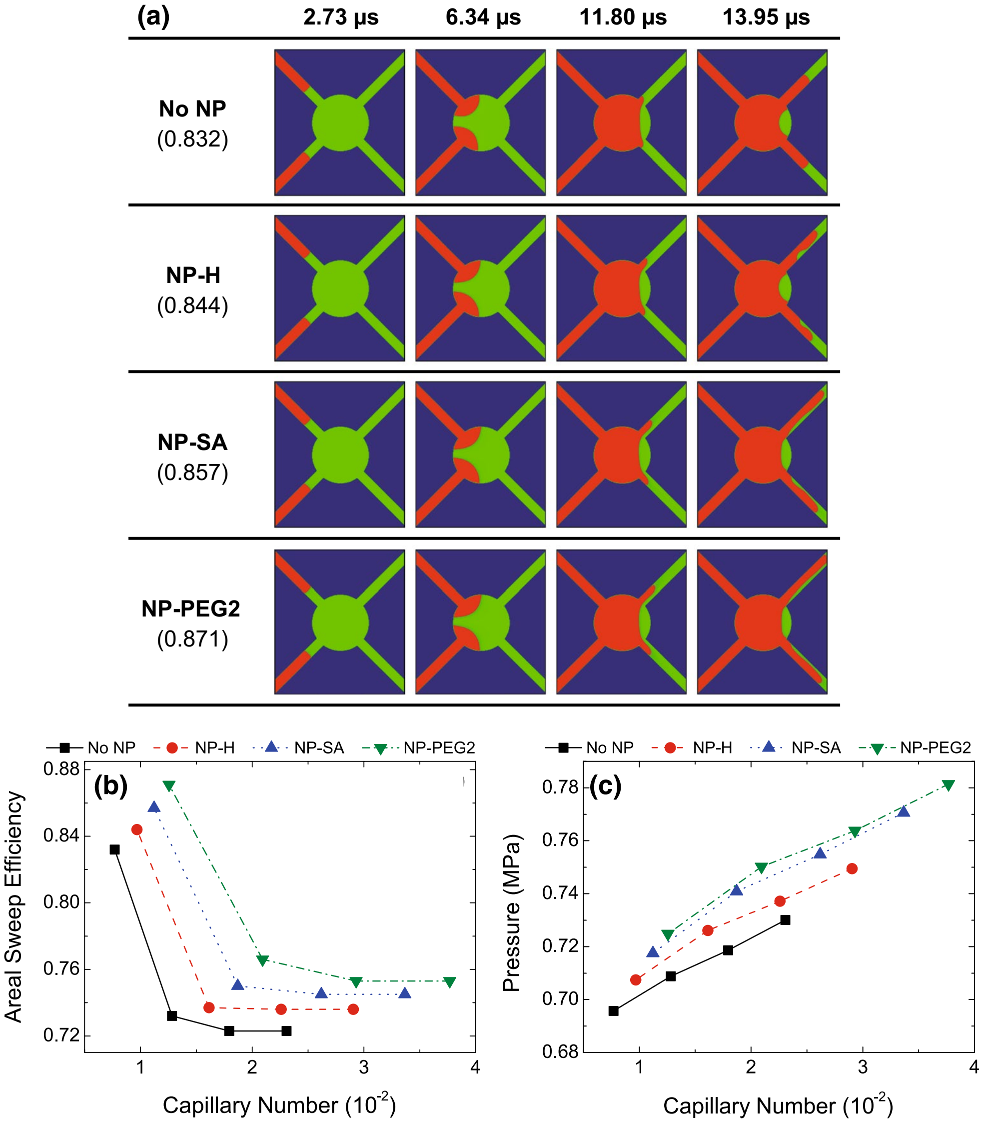

Fig. 7 X-junction pore network model with equal channel widths and a circular pore body. **a** Injection profiles for brine+NP (*red*) solutions into a MMT (*blue*) pore network filled with oil (*green*). Injection rate is 0.003 l_0/t_0, and the areal sweep efficiency attained after 13.95 μs of injection is shown in parenthesis. **b** Areal sweep efficiency as a function of the capillary number. **c** Pressure at the interface. The injection fluids are: (*square*) brine, (*circle*) brine+NP-H, (*up triangle*) brine+NP-SA and (*down triangle*) brine+NP-PEG2. These results are computed at the breakthrough time for brine+NP-PEG2 injection (color figure online)

The time snapshots of Fig. 7a have also shown that the presence of a circular pore body causes the formation of oil droplets inside the pore body. In addition, it is possible to see that the size of droplets decreases with the interfacial tension value between oil and the injection fluids. Therefore, the association of a circular pore body with an injection fluid with high interfacial tension value reduces the fluid displacement efficiency.

An analysis of the areal sweep number as a function of the capillary number is presented in Fig. 7b. In accordance with the previous results, the areal sweep efficiency is larger for injection fluids with lower interfacial tension (brine+NP-PEG2). For the brine+NP-PEG2 solution, an improvement in oil displacement of approximately 4.5 % is seen in relation to a pure brine solution. As the capillary number increases, the areal sweep efficiency decreases. For capillary numbers larger than 1.7×10^{-2}, the areal sweep efficiency became constant. Therefore, the addition of nanoparticles to the brine solution indeed improves the oil displacement.

Due to the symmetry of the channels, the interfacial pressure is similar at both outlet channels. These results are shown in Fig. 7c. Similar to what is previously found, the interfacial pressure increases with the injection rate and with the addition of nanoparticles to the brine solution.

Differently from what was found for the other PNM structures, there are considerable differences for the breakthrough time configurations as the capillary number (injection rates) changes. Figure 8 shows the breakthrough time configurations for all types of injection fluids and different injection rates. As the capillary number increases, the fingering phenomena become more pronounced and the amount of remaining oil considerably increase. For an injection rate of 0.005 l_0/t_0, in systems with larger

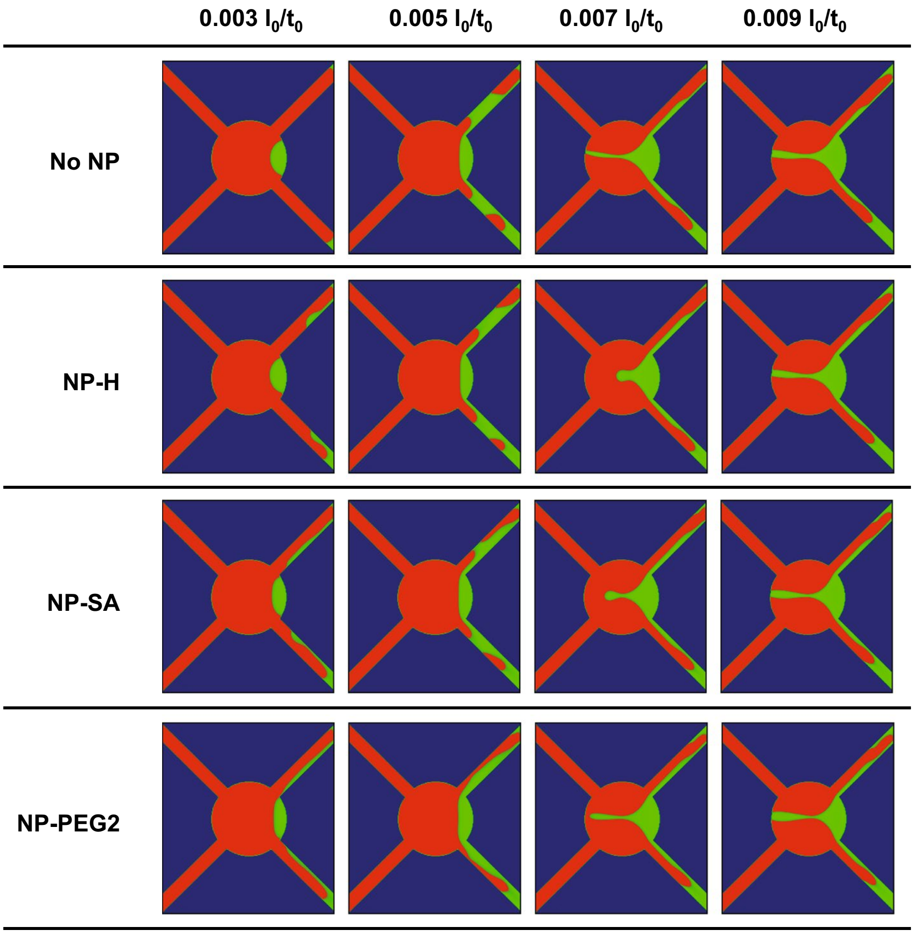

Fig. 8 Breakthrough time configuration for the X-junction pore network model with equal channel widths and a circular pore body. The injected fluid, MMT and oil are shown in *red*, *blue* and *green*, respectively (color figure online)

interfacial tension (No NP, NP–H and NP–SA) the injection force is not strong enough to balance with the interfacial tension and the formation of brine droplets is seen.

Finally, we explore the oil displacement in the X-junction model with unequal channel widths and a central square pore body. The time snapshots of the simulation are shown in Fig. 9a. After 2.54 μs of injection, it is possible to see that, at the inlet part, the fluid displacement is faster for the wider channel, in which the injection fluid front reaches the pore body area first (5.66 μs). At this point, the injection fluid starts to fill the square pore body, and after 8.98 μs, the formation of oil droplets is observed. By the end, after 11.32 μs of injection, the Young–Laplace filling rule is satisfied and the widest channel is filled first.

The largest width of the outlet channel allows the formation of a finger front, as it can be seen at times 8.98 and 11.32 μs in Fig. 9a. Notice that the inclusion of a square pore body prevents the injection fluid to enter the narrowest channel.

The results present in Fig. 9a have also shown that the oil displacement process by brine+NP-SA and brine+NP-PEG2 solutions is much faster than that by the other fluids. For brine+NP-H and pure brine solutions, the breakthrough time is about 12.68 μs. After 11.32 μs of injection, the largest areal sweep numbers are for brine+NP-SA (0.656) and brine+NP-PEG2 (0.669). By comparing these results with the previous PNMs, we may conclude that the inclusion of unequal channel widths and a square pore body will lead to the lowest amount of displaced oil. The finger formation is more pronounced for brine solutions containing nanoparticles, and the Young–Laplace filling rules are satisfied.

Results for the areal sweep number as a function of the capillary number are presented in Fig. 9b. These values are computed for at the breakthrough time for brine+NP-PEG2 injection. An improvement in fluid displacement is seen for injection fluids with nanoparticles. For a brine+NP-PEG2 solution, the fluid displacement efficiency increases more than 5 %. For all injection fluids, as the capillary number increases, the areal sweep efficiency decreases.

The interfacial pressure was evaluated at both outlet channels. Similar to what is found for the X-junction model with unequal channel widths, the fluid front does not reach the narrow channel and values only for the widest channel are computed. These results are shown in Fig. 9c. For all injection fluids, the interfacial pressure increases with the

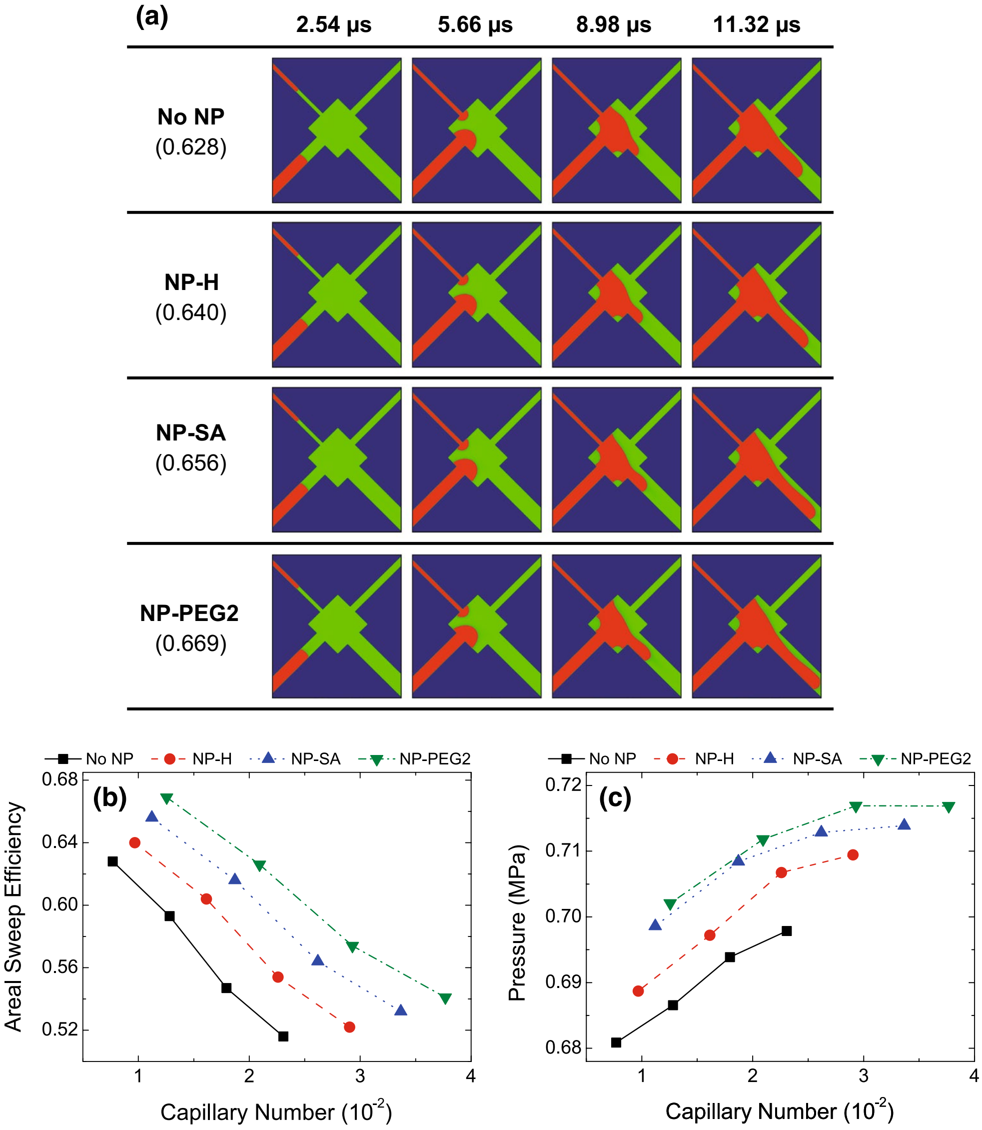

Fig. 9 X-junction pore network model with equal channel widths and a square pore body. **a** Injection profiles for brine+NP (*red*) solutions into a MMT (*blue*) pore network filled with oil (*green*). Injection rate is 0.003 l_0/t_0, and the areal sweep efficiency attained after 11.32 μs of injection is shown in parenthesis. **b** Areal sweep efficiency as a function of the capillary number. **c** Pressure at the interface. The injection fluids are: (*square*) brine, (*circle*) brine+NP-H, (*up triangle*) brine+NP-SA and (*down triangle*) brine+NP-PEG2. These results are computed at the breakthrough time for brine+NP-PEG2 injection (color figure online)

capillary number. Also, the addition of nanoparticles to the brine solution leads to higher interfacial pressure.

In immiscible two phase flow, the viscosity ratio is an important parameter that affects the amount of trapped oil in the pore structure (Dullien 1992). Large viscosity ratios, as seen in our systems ($\nu_o/\nu_b > 5$), make the brine solution likely to finger through the oil, which may result in early breakthrough of fluid, leading to a non-efficient oil displacement (Blunt et al. 1992; Tchelepi et al. (1993)). As observed in our simulations, the reduction in interfacial tension may also result in a more pronounced finger formation and faster fluid displacement as the injection ratio increases. Therefore, the type of nanoparticle and the injection rate must be carefully chosen in order to control the fingering phenomena and obtain an efficient oil displacement process.

6 Conclusions

In this work, we introduce a hierarchical computational protocol to explore the role of interfacial and wetting properties at the nanoscale to the fluid displacement in hydrophilic pore network models at the microscale. MD simulations were employed to investigate how the interfacial tension and the wetting properties of the brine/oil/MMT system changes with the addition of SiO_2 nanoparticles to the brine–oil interface. In order to go beyond the nanoscale, the MD simulations are complemented by LBM simulations, where the physical properties determined via MD calculations are mapped into LBM simulation parameters.

Our MD results indicate that the addition of nanoparticles to the brine solution reduces the interfacial tension between oil and brine, followed by an increase in the contact angle. Results in Table 1 have shown that nanoparticles with different hydrophilic properties will lead to different interfacial tension and contact angles. The lowest interfacial tension and highest contact angle are for the hydrophilic pegylated nanoparticle. Such properties may lead to an enhancement of the oil displacement process in hydrophilic pore structures.

Based on these MD results, LBM simulations have been used to study the oil displacement process in hydrophilic MMT pore network models. For all systems, the Young–Laplace filling rules are obeyed and, as a consequence of the finger formation, the displacement efficiency decreases as the capillary number increases. It was also observed an increase in the interfacial pressure, as the interfacial tension decreases and the contact angle increases (addition of nanoparticles). By comparing the different channel widths, one may conclude that for wider channels, the interfacial forces are more significative and those are a determinant factor in the fluid displacement process. In addition, the presence of unequal channel widths reduces the fluid displacement efficiency in approximately 20 %, since a large amount of oil is retained at the narrow channel. The inclusion of a central pore body allows the formation of trapped oil droplets, which considerably reduces the fluid displacement efficiency. However, the use of brine+NP-PEG2 solution as injection fluid may improve the oil displacement by 5 %. Our results have shown that the reduction in interfacial tension associated with an increase in the contact angle may enhance the oil displacement process in hydrophilic pore systems at the microscale. It must be noted that the present 2D LBM simulations should not be used to fully predict the physical properties of realistic 3D systems. However, they can provide valuable insights of the influence of interfacial tension and contact angle on the fluid behavior.

The proposed computational protocol can be a versatile tool to explore the potentialities of chemical additives, such as nanoparticles, for the oil recovery process and investigate the effects of interfacial tension and wetting properties on the fluid behavior at both nano- and microscales.

Acknowledgments This work was supported by the Advanced Energy Consortium: http://www.beg.utexas.edu/aec/ Member companies include BP America Inc., BG Group, Petrobras, Repsol, Schlumberger, Statoil, Shell, and Total. The authors also acknowledge the financial support provided by the Brazilian agencies CAPES, CNPq, and FAPESP and the computational support from CENAPAD/SP and UFABC.

References

Alejandre J, Chapela GA, Bresme F, Hansen JP (2009) The short range anion-H interaction is the driving force for crystal formation of ions in water. J Chem Phys 130:174505-1-10

Andersen HC (1980) Molecular dynamics simulations at constant pressure and/or temperature. J Chem Phys 72:2384–2393

Amott E (1956) Observations relating to the wettability of porous rock. Trans AIME 216:156–162

Benjamin I (1997) Molecular structure and dynamics at liquid-liquid interfaces. Ann Rev Phys Chem 48:407–451

Berthelot D (1898) Compte rendus hebdomadaires des seances de lacademie des sciences. Acad des Sci Bachelier Paris 126:1703–1706

Biben T, Joly L (2008) Wetting on nanorough surfaces. Phys Rev Lett 100:186103-1–4

Blunt M, King MJ (1992) Simulation and theory of two-phase flow in porous media. Phys Rev A 46:7680

Bonn PD, Eggers J, Indekeu J, Meunier J, Rolley E (2009) Wetting and spreading. Rev Mod Phys 81:739–805

Boukellal H, Selimović S, Jia Y, Cristobalb G, Fraden S (2009) Simple, robust storage of drops and fluids in a microfluidic device. Lab Chip 9:331–338

Brindley GW, Brown G (1980) Crystal structures of clay minerals and their X-ray identification. Mineralogical Society, London

Brooks BR et al (2009) CHARMM: the biomolecular simulation program. J Comp Chem 30:1545–1615

Buckley JS, Fan T (2007) Crude oil/brine interfacial tensions. Petrophysics 48:175–185

Buckley JS (1991) Multiphase displacements in micromodels. In: Interfacial phenomena in petroleum recovery. Marcel Dekker Inc, New York, pp 157–189

Chandler D (2007) Physical chemistry: oil on troubled waters. Nature 445:831–832

Chapmana EM, Yanga J, Crawshawa JP, Boek ES (2013) Pore scale models for imbibition of CO_2 analogue fluids in etched microfluidic junctions from micro-model experiments and direct LBM flow calculations. Energy Procedia 37:3680–3686

Chattoraj DK, Birdi KS (1984) Adsorption and the Gibbs surface excess. Plenum Publishing Company, New York

Chen S, Doolen GD (1998) Lattice Boltzmann method for fluid flows. Ann Rev Fluid Mech 30:329–364

Chu EC, Aksimentiev A, Schulten K (2006) Water-silica force field for simulating nanodevices. J Phys Chem B 110:21497–21508

Coon ET, Porter ML, Kang Q (2014) Taxila LBM: a parallel, modular lattice Boltzmann framework for simulating pore-scale flow in porous media. Comput Geosci 18:17–27. https://software.lanl.gov/taxila

Cygan RT, Liang JJ, Kalinichev AG (2004) Molecular models of hydroxide, oxyhydroxide, and clay phases and the development of a general force field. J Phys Chem B 108:1255–1266

de Lara LS, Michelon MF, Miranda CR (2012a) Molecular dynamics studies of fluid/oil interfaces for improved oil recovery processes. J Phys Chem B 116:14667–14676

de Lara LS, Michelon MF, Metin CO, Nguyen QP, Miranda CR (2012b) Interface tension of silica hydroxylated nanoparticle with brine: a combined experimental and molecular dynamics study. J Chem Phys 136:164702-1-8

de Serio M, Mohapatra H, Zenobi R, Deckert V (2006) Investigation of the liquid–liquid interface with high spatial resolution using near-field Raman spectroscopy. Chem Phys Lett 417:452–456

Du Q, Freysz E, Shen YR (1994) Surface vibrational spectroscopic studies of hydrogen bonding and hydrophobicity. Science 264:826–828

Dullien FAL (1992) Fluid transport and pore structure. Academic Press, San Diego

Evans DJ, Morriss GP (1990) Statistical Mechanics of Non Equilibrium Liquids. Academic Press, London 1990, Theoretical Chemistry Monograph Series

Gavryushov S (2007) Dielectric saturation of the ion hydration shell and interaction between two double helices of DNA in mono- and multivalent electrolyte Solutions: foundations of the ϵ-modified Poisson-Boltzmann theory. J Phys Chem B 111:5264–5276

Ghoufi A, Goujon F, Lachet V, Malfreyt P (2008) Surface tension of water and acid gases from Monte Carlo simulations. J Chem Phys 128:154716–154731

Green MS (1954) Markoff random processes and the statistical mechanics of time-dependent phenomena. J Chem Phys 22:398–413

He X, Zou Q, Luo LS, Dembo M (1997) Analytic solutions of simple flows and analysis of nonslip boundary conditions for the lattice Boltzmann BGK model. J Stat Phys 87:115–136

Hockney E (1989) Computer simulation using particles. Adam Hilger, New York

Hoover WG (1985) Canonical dynamics: equilibrium phase-space distributions. Phys Rev A 31:1695–1697

Hore DK, Walker DS, Richmond GL (2008) Water at hydrophobic surfaces: when weaker is better. J Am Chem Soc 130:1800–1801

Jang SS, Lin ST, Maiti PK, Blanco M, Goddard WAJ, Shuler P, Tang Y (2004) Molecular dynamics study of a surfactant-mediated decane-water interface: effect of molecular architecture of alkyl benzene sulfonate. J Phys Chem B 108:12130–12140

Jungwirth P, Finlayson-Pitts BJ, Tobias D (2006) Introduction: structure and chemistry at aqueous interfaces. J Chem Rev 106:1137–1139

Koplik J, Banavar JR (1995) Continuum deductions from molecular hydrodynamics. Annu Rev Fluid Mech 27:257–292

Kubo R (1957) Statistical-mechanical theory of irreversible processes. J Phys Soc Jpn 12:570–586

Kunieda M, Nakaoka K, Liang Y, Miranda CR, Ueda A, Takahashi S, Okabe H, Matsuoka T (2010) Self-accumulation of aromatics at the oil-water interface through weak hydrogen bonding. J Am Chem Soc 132:18281–18286

Lambert J, Hergenröder R, Suter D, Deckert V (2009) Probing liquidliquid interfaces with spatially resolved NMR spectroscopy. Angew Chem Int Ed 48:6343–6345

Lenormand R, Zarcone C, Sarr A (1983) Mechanisms of the displacement of one fluid by another in a network of capillary ducts. J Fluid Mech 135:337–353

Li Y, Xu J, Li D (2010) Molecular dynamics simulation of nanoscale liquid flows. Microfluid Nanofluid 9:1011–1031

Lorentz HA (1881) Ueber die anwendung des satzes vom virial in der kinetischen theorie der gase. Ann der Phys 248:127–136

Makimura D, Metin C, Kabashima T, Matsuoka T, Nguyen QP, Miranda CR (2010) Combined modeling and experimental studies of hydroxylated silica nanoparticles. J Mater Sci 45:5084–5088

McElfresh PM, Wood M, Ector D (2012) Stabilizing nano particle dispersions in high salinity, high temperature downhole environments. SPE 154758-MS

Metin CO, Rankin KM, Nguyen QP (2014) Phase behavior and rheological characterization of silica nanoparticle gel. Appl Nanosci 4:93–101

Michael D, Benjamin I (1995) Solute orientational dynamics and surface roughness of water/hydrocarbon interfaces. J Phys Chem 99:1530–1536

Miranda CR, de Lara LS, Tonetto BC (2012) Stability and mobility of functionalized silica nanoparticles for enhanced oil recovery applications. SPE 157033-MS

Mitrinovic DM, Tikhonov AM, Li M, Huang ZQ, Schlossman ML (2000) Noncapillary-wave structure at the water-alkane interface. Phys Rev Lett 85(3):582–585

Murray DK (2010) Differentiating and characterizing geminal silanols in silicas by ^{2}9Si NMR spectroscopy. J Colloid Interface Sci 352:163–170

Navrotsky A (2003) Zeolites: ordered, disordered, collapsed. Nat Mater 2:571–572

Nomoto T, Onishi H (2007) Fourth-order coherent raman spectroscopy in a time domain: applications to buried interfaces. PCCP 9:5515–5521

Nosé S (1984) A unified formulation of the constant temperature molecular dynamics methods. J Chem Phys 81:511–519

Petersen KS, Christensen PL (2007) Phase behavior of petroleum reservoir fluids. CRC, Boca Raton

Plimpton S (1995) Fast parallel algorithms for short-range molecular dynamics. J Comput Phys 117:1-19. http://lammps.sandia.gov

Porter ML, Coon ET, Kang Q, Moulton JD, Carey JW (2012) Multicomponent interparticle-potential lattice Boltzmann model for fluids with large viscosity ratios. Phys Rev E 86:036701-1–036701-8

Rigo VA, de Lara LS, Miranda CR (2014) Energetics of formation and hydration of functionalized silica nanoparticles: an atomistic computational study. App Surf Sci 292:742–749

Scatena LF, Brown MG, Richmond GL (2001) Water at hydrophobic surfaces: weak hydrogen bonding and strong orientation effects. Science 292:908–912

Sondjaja HR, Hatton TA, Tam KC (2008) Self-assembly of poly(ethylene oxide)-block-poly(acrylic acid) induced by $CaCl_2$: mechanistic study. Langmuir 24:8501–8506

Song J, Choi M (2002) Stability of elongated and compact types of structures in SiO_2 nanoparticles. Phys Rev B 65:241302-1–241302-4

Succi S (2001) The lattice Boltzmann equation. Oxford University Press, Oxford

Sukop MC, Thorne DT Jr (2006) Lattice Boltzmann modeling. Springer, Delft

Talu O, Myers AL (2001) Molecular simulation of adsorption: Gibbs dividing surface and comparison with experiment. AIChE J 47:1160–1168

Tchelepi HA, Orr FM Jr, Rakotomalala N, Salin D, Woumeni R (1993) Dispersion, permeability heterogeneity and viscous fingering: acoustic experimental observations and particle tracking simulations. Phys Fluids 5:1558–1574

Thompson AP, Plimpton SJ, Mattson W (2009) General formulation of pressure and stress tensor for arbitrary many-body interaction potentials under periodic boundary conditions. J Chem Phys 131:154107–154112

Ushikubo FY, Birribilli FS, Oliveira DRB, Cunha RL (2014) Y- and T-junction microfluidic devices: effect of fluids and interface properties and operating conditions. Microfluid Nanofluid 17:711–720

Varnik F, Baschnagel J, Binder K (2000) Molecular dynamics results on the pressure tensor of polymer films. J Chem Phys 113:4444–4453

Wasan DT, Nikolov AD (2003) Spreading of nanofluids on solids. Nature 423:156–159

Wolf-Gladrow DA (2000) Lattice-gas cellular automata and lattice Boltzmann models. Springer, Berlin

Wörner M (2012) Numerical modeling of multiphase flows in microfluidics and micro process engineering: a review of methods and applications. Microfluid Nanofluid 12:841–886

Zhang L, Zhang Z, Wang P (2012) Smart surfaces with switchable superoleophilicity and superoleophobicity in aqueous media: toward controllable oil/water separation. NPG Asia Mater 4:e8

Zhang J (2011) Lattice Boltzmann method for microfluidics: models and applications. Microfluid Nanofluid 10:1–28

Zhang T, Davidson A, Bryant SL, Huh C (2010) Nanoparticle-stabilized emulsions for applications in enhanced oil recovery. SPE 129885-MS

Zhang Y, Feller SE, Brooks BR, Pastor RW (1995) Computer simulation of liquid/liquid interfaces. I. theory and application to octane/water. J Chem Phys 103:10252–10266